RSC Advances

PAPER

View Article Online
View Journal | View Issue

Cite this: *RSC Adv.*, 2015, **5**, 51067

Photocatalytic inactivation of *E. Coli* by ZnO–Ag nanoparticles under solar radiation

Sangeeta Adhikari,[a] Aditi Banerjee,[b] Neerugatti KrishnaRao Eswar,[b] Debasish Sarkar[a] and Giridhar Madras*[b]

Porous and fluffy ZnO photocatalysts were successfully prepared *via* simple solution based combustion synthesis method. The photocatalytic inactivation of *Escherichia coli* bacteria was studied separately for both Ag substituted and impregnated ZnO under irradiation of natural solar light. A better understanding of substitution and impregnation of Ag was obtained by Raman spectrum and X-ray photoelectron analysis. The reaction parameters such as catalyst dose, initial bacterial concentration and effect of hydroxyl radicals *via* H_2O_2 addition were also studied for ZnO catalyst. Effective inactivation was observed with 0.25 g L^{-1} catalyst loading having 10^9 CFU mL^{-1} bacterial concentration. With an increase in molarity of H_2O_2, photocatalytic inactivation was enhanced. The effects of different catalysts were studied, and highest bacterial killing was observed by Ag impregnated ZnO with 1 atom% Ag compared to Ag substituted ZnO. This enhanced activity can be attributed to effective charge separation that is supported by photoluminescence studies. The kinetics of reaction in the presence of different scavengers showed that reaction is significantly influenced by the presence of hole and hydroxyl radical scavenger with high efficiency.

Received 10th April 2015
Accepted 1st June 2015

DOI: 10.1039/c5ra06406f

www.rsc.org/advances

1. Introduction

Nanostructures offer tailored and improved properties for versatile applications owing to their unique physicochemical properties such as large surface to volume ratios and nanosize dimensions.[1,2] Microbial contamination has become a serious issue of debate due to the spread of the antibiotic resistant infections.[3] Coliforms are present in the environment which makes their presence obvious in contaminated water contributes to diarrheal diseases.[4,5] Therefore, antimicrobial agents in the form of powders, organic–inorganic nanocomposite coating or coating on cellulose fibers are studied extensively.[6] Recently, inorganic materials like TiO_2,[7] SiO_2,[8] ZnO (ref. 9) and silver nanoparticles[10] have been engineered to impart strong antimicrobial properties.

In this respect, nanocrystalline ZnO is a promising material with exciton binding energy of 60 meV.[11,12] It imparts superior chemical stability with lower toxicity that makes it appropriate for applications such as photocatalysts, solar cells, *etc.*[13–15] Moreover, ZnO nanoparticles act as bacteriocide and can restrain the growth of both Gram-negative and Gram-positive bacteria with minimum damage to human cells.[16–18] Gram positive and negative bacterium such as *Bacillus atrophaeus* and *Escherichia coli* (*E. coli*) were inactivated by hydrothermally synthesized ZnO nanorods.[9] The photocatalytic bacterial killing takes place *via* excitation of semiconductor material forming electron–hole pair, which eventually disrupts the cell membrane and damages the cell wall due to peroxidation of the unsaturated phospholipids through short-lived but highly active radicals.[19,20]

Performance tuning and augmentation of activity by doped ZnO nanocrystals have been of research interest.[21,22] Various studies have been employed to tune the properties of the material that depends on the synthesis method for inhibition of bacterial growth. Among the solution based methods, the combustion process produces highly pure porous nanopowders with easy control over composition, low processing temperature, and good homogeneity. Moreover, this method yields powder with fairly high surface area and also large scale fabrication is possible without any sophisticated instrumentation.[23,24]

Surface modification of the catalyst has a strong influence on the photocatalytic bacterial killing.[25] Thus, ZnO is coupled with various elemental/compounded materials to prevent the recombination of electron–hole pair upon light interaction with the surface to obtain better efficacy. Ag is a potential material with bactericide properties. ZnO is an n-type semiconductor that becomes an effective p-type semiconductor upon Ag doping that changes the optoelectronic properties that influence photocatalytic activity. Recently, microwave technique was employed to synthesize micro/nanospheres of ZnO/Ag for inactivation of *E. coli* and photocatalytic degradation of methyl orange dye.[26] Fan's group[27] has reported the formation of

[a]*Department of Ceramic Engineering, National Institute of Technology, Rourkela, India*
[b]*Department of Chemical Engineering, Indian Institute of Sciences, Bangalore, India. E-mail: giridharmadras@gmail.com; Tel: +91-080-2293-2321*

unique honeycomb Ag/ZnO heterostructures and their photocatalytic efficiency against Rhodamine B. However, in this study, we have explored how silver substitution and impregnation in ZnO affects the photocatalytic killing of bacteria in comparison to the synthesized ZnO.

Thus, in the present work, we report the preparation of ZnO by a solution combustion method using alanine as fuel. The study and comparison of the photoactivity of Ag-substituted and Ag-impregnated ZnO has been carried out. Bacterial inactivation rate in the presence of H_2O_2 and other scavengers have also been studied to understand the inactivation mechanism. We further compare the activity of the synthesized material with the commercial catalyst.

2. Materials and methods

2.1. Materials

The precursor zinc nitrate hexahydrate ($Zn(NO_3)\cdot 6H_2O$) and hydrogen peroxide (30%) was purchased from Merck (India). Other chemicals, such as-L-alanine ($CH_3CH(NH_2)COOH$) and silver nitrate ($AgNO_3$), were purchased from S.D. Fine Chemicals (India). Millipore double distilled water was used for all the experiments.

2.2. Catalysts synthesis

Pristine ZnO nanopowder catalyst was prepared *via* solution combustion method. The typical synthesis process includes dissolving stoichiometric quantities of oxidizer zinc nitrate hexahydrate and the fuel L-alanine in a minimum amount of water. The mixture is stirred for 30 min for homogeneous mixing. The aqueous solution was subjected to combustion in a preheated muffle furnace at 370 °C for a short period to obtain ZnO nanopowders. For 1 atom % Ag-substituted ZnO (ZnO–Ag sub), stoichiometric amount of $Zn(NO_3)\cdot 6H_2O$, alanine, and $AgNO_3$ were taken in the muffle furnace at 370 °C. On the other hand, Ag-impregnated ZnO (ZnO–Ag imp) was prepared by impregnating metal (1 atom %) on the pre-synthesized ZnO surface. For the preparation of ZnO–Ag imp, combustion synthesized ZnO was dispersed in water, and the appropriate amount of $AgNO_3$ was introduced drop by drop into the system containing hydrazine hydrate. The process was followed by drying, in order to recover the catalyst at 150 °C for 24 h. Zinc oxide (~100 nm, Sigma Aldrich) was used as the commercial catalyst and Ag was impregnated in this catalyst by the same method and this was designated as Zno Ag imp (comm). This catalyst was used for comparison of photocatalytic activity with the prepared materials.

2.3. Catalysts characterization

The prepared catalysts were characterized by various analytical techniques. The X-ray diffraction (XRD) patterns of the catalyst were measured using Ni filtered CuKα radiation (Rigaku, Ultima IV system). Morphological analyzes were carried by FESEM (NOVA NANOSEM FEI-450 system) and TEM (JEOL JEM-2100 system). Specific surface areas of the catalysts were determined using N_2 as adsorbate in Quatachrome Autosorb, USA. X-ray photoelectron spectra (XPS) of these samples were recorded with AXIS Ultra X-ray photoelectron spectroscopy. UV-DRS measurement was carried using Shimadzu spectrophotometer (UV-2450) and photoluminescence (PL) spectra of the prepared photocatalysts were measured using Hitachi F-4500 spectrofluorimeter.

2.4. Microorganisms and growth media

The current study used Gram negative *Escherichia coli* (*E. coli*) K-12 (MG 1655) micro-organism as the host micro-organism. The bacterial strain was obtained locally from the culture collections. The bacteria were grown aerobically in Luria–Bertani (LB) media (HiMedia, India). Bacterial culture was prepared by the constant agitation of fresh inoculums in 100 mL of media in an incubator with constant shaking at 200 rpm (Scigenic biotech, India). In order to monitor the growth of the cells, optical density was measured at 600 nm. The exponential growth phase was used for cell culture collection. It was further centrifuged at 3500 rpm for 20 min followed by washing twice with germ-free deionized water. The re-suspension of bacterial cell plates in 100 mL deionized water was done. An initial *E. coli* concentration used was approximately 10^9 CFU mL^{-1} (CFU – colony forming units). It was used immediately without storing for all the photocatalytic inactivation experiments. Solid medium of agar plates was prepared using LB media and 2% agar powder (HiMedia, India). The agar plates were used in the viable count method for the analysis of inactivated bacterial samples. Further details of the bacterial strain, growth media and details of the experiments can be found elsewhere.[28]

2.5. Photochemical inactivation experiments

The antimicrobial experiments were carried under natural sunlight. A batch of solution containing bacteria-catalyst for which the catalyst activity is to be compared was simultaneously exposed to sunlight and the solutions were continuously stirred with a magnetic stirrer. All the experiments were carried out between 11 am to 3 pm since the solar intensity fluctuations are minimal in that duration and the variation in the solar intensity was recorded with a radiometer (Eppley PSP 32483F3, Newport, USA) and the average solar intensity was 0.753 kW m^{-2}.

2.6. Bacterial sample analysis

All the glasswares and plastics used for the preparation of medium, during photocatalytic experiments and inactivation study were autoclaved at 120 °C for 4 h. For antimicrobial activity determination of catalyst, 50 mL of the bacterial solution of known bacterial concentration was taken in 100 mL beaker with known catalyst loading and placed under sunlight. For analysis, 100 μl of suspension was collected at fixed intervals from the thoroughly stirred solution and the bacterial count was performed. The cell counting was done by standard viable count method/plate count method. The suspension collected was successively diluted in deionized water for the final count to be in between 10–100 CFU mL^{-1}. A suspension of 100 μl was spread on nutrient agar plates. The agar plates containing inactivated samples were incubated overnight. The

fully grown colonies on plates were counted and recorded. The number of colonies forming units (CFU's) was counted considering the dilution factor after incubation at 37 °C for 24 h. The respective data are the average values obtained from triplicate runs.

2.7. Bacterial sample analysis

The stability of the catalyst was confirmed by conducting deactivation studies. Experiments were conducted with the ZnO–Ag (imp) with a loading of 0.25 g L^{-1}. Once the bacterial inactivation was complete in 2 h, the reaction was stopped and the second cycle was started after making the initial concentration of *E. coli* to ~1.1 × 10^9 CFU mL^{-1}. Similarly, the third cycle was also carried out. The catalyst is taken at the end of the first cycle and used for the second cycle and the catalyst at the end of the second cycle was used for the third cycle.[29] This was repeated for seven cycles.

3. Results and discussion

3.1. Catalyst characterizations

3.1.1. Phase analysis. The X-ray diffraction pattern for pristine zinc oxide, silver substituted and impregnated zinc oxides were shown in Fig. 1. The solution combustion prepared zinc oxide has a hexagonal structure with *P*63*mc* space group symmetry. The peaks at 31.71°, 34.32°, 36.16°, 47.42°, 56.47°, 62.80°, 66.32°, 67.85°, 68.97°, 72.45° and 76.91° were identified as (100), (002), (101), (102), (110), (103), (200), (112), (201), (004) and (202) planes, respectively according to the JCPDS: 01-076-0704. From the diffraction patterns of silver substituted and impregnated zinc oxide samples, specific peaks observed at 38.14°, 44.24°, 64.41° correspond to Ag having cubic structure with $Fm\bar{3}m$ space symmetry according to JCPDS: 01-087-0717. The peak intensity for Ag in substituted catalyst is lesser compared to impregnated sample. Therefore, the presence of Ag in the X-ray pattern suggests that the silver has been successfully substituted and impregnated to zinc oxide nanoparticles. Substitution and impregnation of silver in zinc oxide can be well understood by Raman scattering and XPS analyzes.

3.1.2. Raman analysis. Fig. 2 shows the Raman scattering of pristine zinc oxide, silver substituted and silver impregnated zinc oxide catalysts. Zinc oxide belongs to wurtzite structure having C_{6v} point group symmetry. Among A_1, E_1, E_2 and B_1 modes, all modes are active except B_1. Typical zinc oxide consists of couple of polar branches splitting as longitudinal and transversal components because of longitudinal optical phonons. Modes corresponding to Zn lattice vibrations are denoted as E_{2L} whereas for oxygen atoms it will be represented as E_{2H}, A_1 and E_2 modes can be observed, rest are forbidden modes based on Raman selection rules. Raman peak at 436 cm^{-1} can be matched to the fundamental E_{2H} mode of zinc oxide. Similarly, peak at 650 cm^{-1} correspond to $2(E_{2H}–E_{2L})$ modes of Raman scattering. The peak approximately at 330 cm^{-1} corresponds to $3(E_{2H}–E_{2L})$ modes. Both $2(E_{2H}–E_{2L})$ and $3(E_{2H}–E_{2L})$ arises because of multi-phonon scattering modes. The intensity of the peak at 436 cm^{-1} decreases from pristine ZnO to Ag substituted ZnO. This is because of incorporation of Ag dopants in zinc oxide lattice that affects the crystallinity and also the translational crystal symmetry. The substituted atoms might exhibit local or gap modes that are localized at its specific site, since they do not resonate to the host lattices vibrations. The broad Raman peaks approximately between 380 cm^{-1} and 390 cm^{-1} and 550 cm^{-1} to 580 cm^{-1} are due to the presence of silver atoms. These silver atoms produce polar branches of A_1 (TO) and A_1 (LO) fundamental modes of Raman scattering.[30,31]

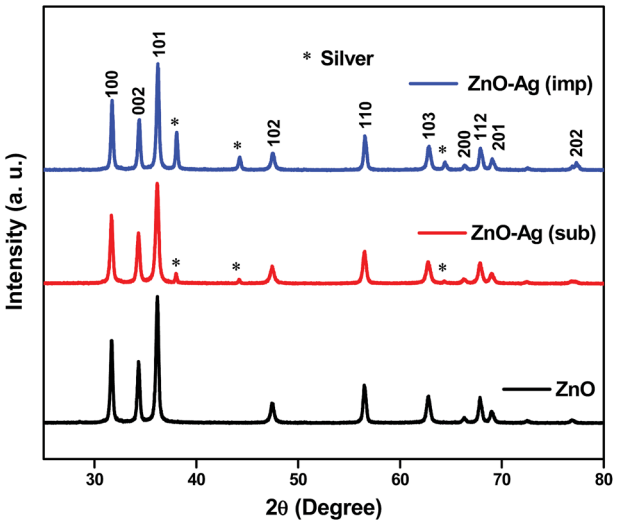

Fig. 1 Composite XRD patterns of synthesized catalysts.

3.1.3. XPS analysis. The X-ray photoelectron spectroscopy analyses of zinc oxide, silver substituted and impregnated zinc oxide were shown in Fig. 3. The carbon C-1s XPS peak analyzed at 284.3 eV as shown in Fig. 3(a), corresponds to adventitious carbon on the surface of ZnO and also peak 287 eV matched to C–O–C bonds, which could be due to the carbon content existing from solution combustion preparation. The O-1s spectra

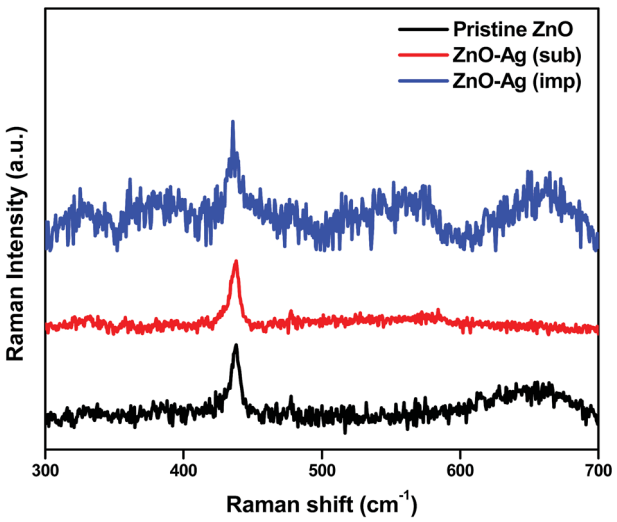

Fig. 2 Raman spectra of pristine ZnO, ZnO–Ag (sub) and ZnO–Ag (imp) nanopowders.

recorded for pristine ZnO sample (Fig. 3(b)) showed three distinct peaks at 529 eV, 531 eV and 532 eV that can be related to lattice oxygen, oxygen defects and chemisorbed oxygen species or hydroxyl species on zinc oxide, respectively. The O-1s spectra of Ag doped ZnO (Fig. 3(c)) showed no chemisorbed or hydroxyl species. This can also be corroborated with the lesser photoactivity of Ag substituted ZnO. There is no significant change in the peak positions of Zn-2p in pristine, substituted and impregnated samples as shown in Fig. 3(d). The Zn $3d_{3/2}$ and $3d_{5/2}$ were recorded and deconvoluted at 1044 eV and 1020 eV, respectively. The silver in the substituted ZnO existed in Ag^{+} ionic state proving the substitution of Ag ions into zinc oxide lattice. The Ag-3d peak at 367 eV and 373 eV can correspond to Ag-$3d_{5/2}$ and Ag-$3d_{3/2}$ ionic states of Ag, as shown in Fig. 3(e). However, the silver in Ag impregnated ZnO existed in metallic state or ground state that can be seen from Fig. 3(f). The peaks at 369 eV and 375 eV correspond to the 3d ground states of silver. Thus, based on this analysis, a better outlook to substitution and impregnation of Ag was obtained.[32,33]

3.1.4. Morphological analysis. The typical FESEM images of the as prepared pristine zinc oxide, silver substituted and impregnated zinc oxide are shown in Fig. 4. Furthermore, the distribution of Ag, Zn, and O was studied for prepared silver substituted (ZnO–Ag (sub)) and impregnated (ZnO–Ag (imp)) catalysts by elemental mapping of the FESEM images. Fig. 4(a) shows the FESEM images of pristine zinc oxide. It was observed that zinc oxide nanopowders are highly porous and spongy in nature. On the other hand, FESEM image of silver substituted

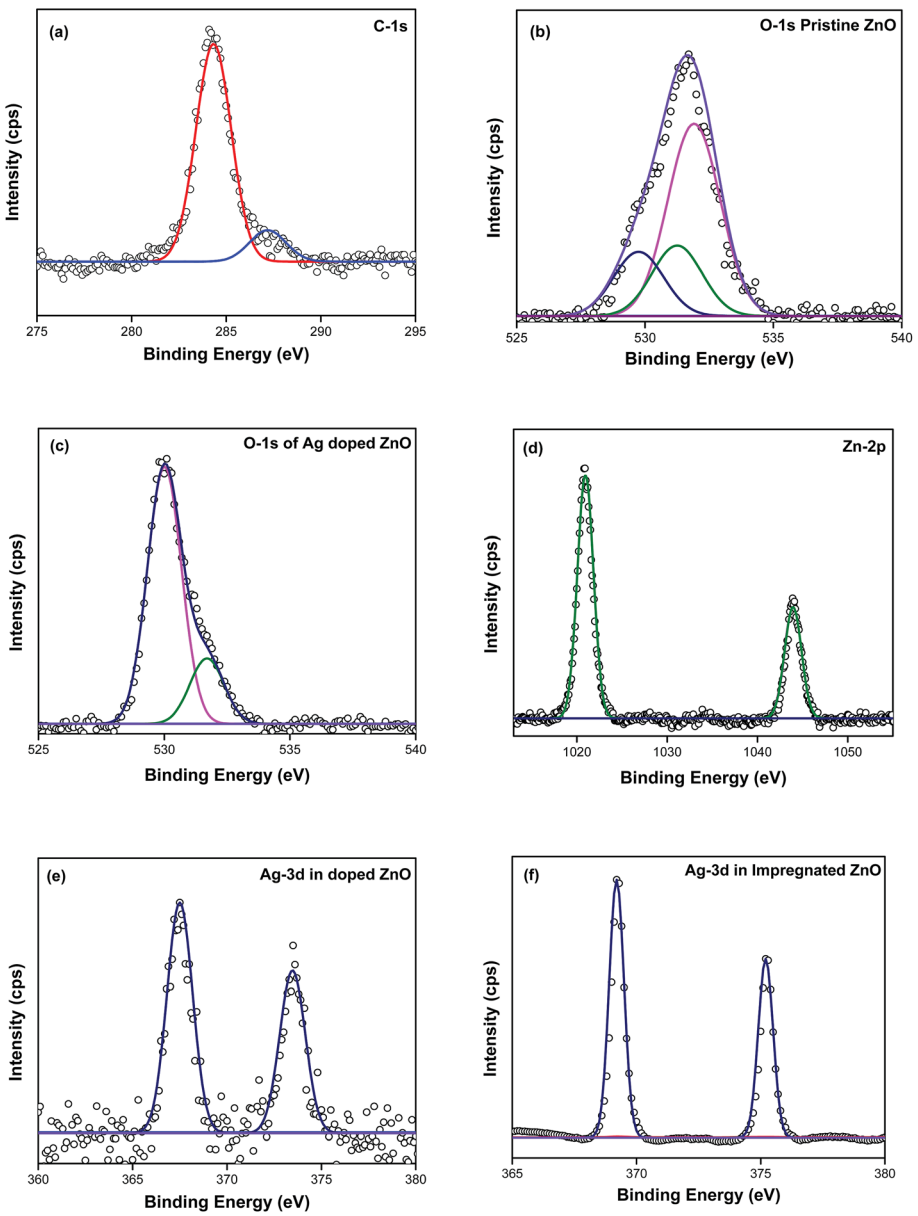

Fig. 3 X-ray photoelectron spectra of (a) C-1s of ZnO, (b) O-1s of pristine ZnO, (c) O-1s of ZnO–Ag (sub), (d) Zn-2p of ZnO, (e) Ag-3d of ZnO–Ag (sub) and (f) Ag-3d of ZnO–Ag (imp).

ZnO (Fig. 4(b)) visually did not evidence the substitution of silver as it exhibited similar porous and fluffy nature, unlike zinc oxide. Elemental mapping of Ag-substituted ZnO showed the presence of zinc (green), silver (red) and oxygen (blue), respectively. It is evident that Zn and O are higher in density in comparison to Ag, and there is a non-homogeneous distribution of Ag over the considered region in the catalyst. Impregnation of silver on ZnO is well understood in Fig. 4(c) with small spherical particles sitting on the surface of porous ZnO. Surface with silver covering shows a decrease in zinc and oxygen density. Uniform distribution of Ag is observed in the region for silver impregnated samples.

In order to better understand the impregnated distribution of silver in ZnO, transmission electron microscopy with HRTEM and SAED has been carried as shown in Fig. 5(a–d). TEM image of the silver impregnated zinc oxide clearly depicts non-uniform size particles with some nearly spherical particles as seen in Fig. 5(a). The porous zinc oxide mass constitutes agglomeration of small particles during combustion process where as silver remains as high dense particle probably due to its high atomic number. The average particle size from TEM image is found to be ~35 nm. The SAED pattern shown in Fig. 5(b) shows number of distinct concentric rings with superimposed bright spots. In Fig. 5(c), we can see few particles softly agglomerated, indicating the particle size of silver to be approximately 20 nm. HRTEM image of Ag/ZnO heterojunction of the boxed region in Fig. 5(c) is shown in Fig. 5(d). The lattice fringes of ZnO are observed to be 0.27 nm consistent with the (100) reflection and lattice distance of 0.23 nm corresponds to the *d*-spacing of the (111) crystal plane of Ag, as shown in Fig. 5(d).

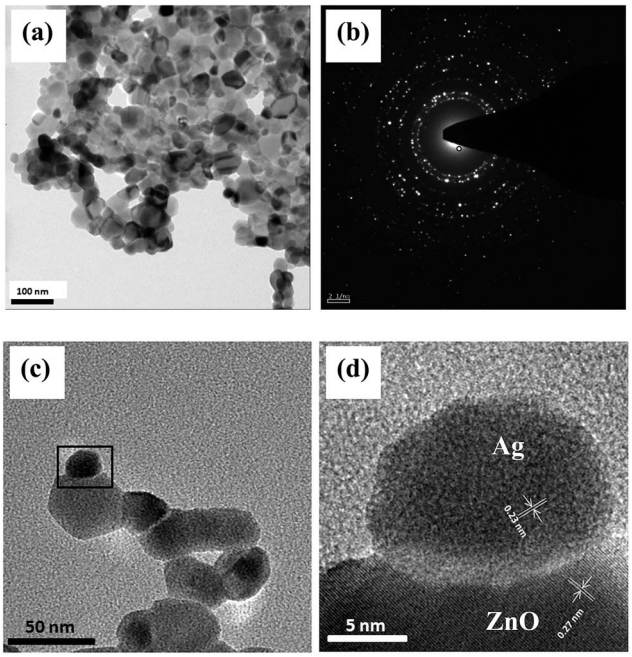

Fig. 5 (a) TEM image, (b) SAED pattern and (c) HRTEM image of ZnO–Ag (imp) nanopowders (d) lattice fringes obtained from the heterojunction from the box shown in (c).

3.1.5. UV-Vis DRS & band gap determination. Fig. 6 shows the UV-DRS spectra of zinc oxide, silver substituted and impregnated zinc oxide powders. The presence of silver sharpens the band gap absorption in comparison to the pristine zinc oxide. Silver work function ranges in between the conduction band (CB) and valence band (VB) of ZnO that accelerates the light absorption capacity. The absorption edge is observed between 360–385 nm which is blue shifted due to substitution and impregnation of Ag as shown in Fig. 6(a). This blue shift is attributed to quantum confinement effects due to reduced size of particles. Estimation of band gap energy is carried using Tauc plot that uses the value obtained from extrapolated linear slope to photon energy as shown in Fig. 6(b). The band gap of pristine zinc oxide, silver substituted and silver impregnated is found to be 2.75 eV, 3.11 eV and 3.21 eV, respectively. The band gap of zinc oxide decreases as a result of increase in oxygen vacancies that are induced during the rapid combustion process. The band gap of Ag loaded ZnO increases due to phenomenon known as Moss–Burstein shift. Hence, Ag loaded zinc oxide shows higher band gap energy.[34]

3.2. Photocatalytic inactivation of bacteria

3.2.1. Effect of catalyst loading. The catalyst loading plays a critical role in photocatalytic inactivation of microorganisms.[35]

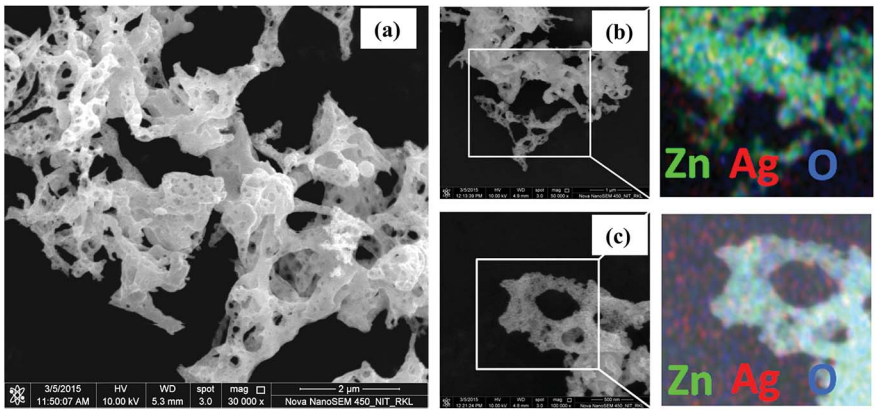

Fig. 4 FESEM images of (a) pristine ZnO nanopowders, (b) ZnO–Ag (sub) and (c) ZnO–Ag (imp) with EDS-elemental mapping of composites.

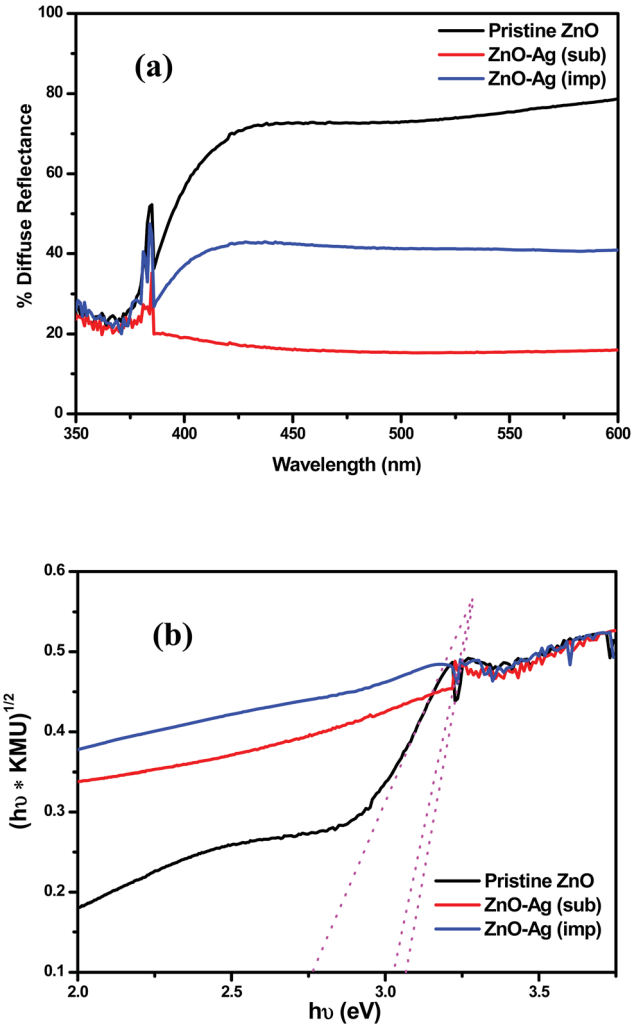

Fig. 6 UV-DRS and band gap determination of ZnO, ZnO–Ag (imp) and ZnO–Ag (subs) catalysts.

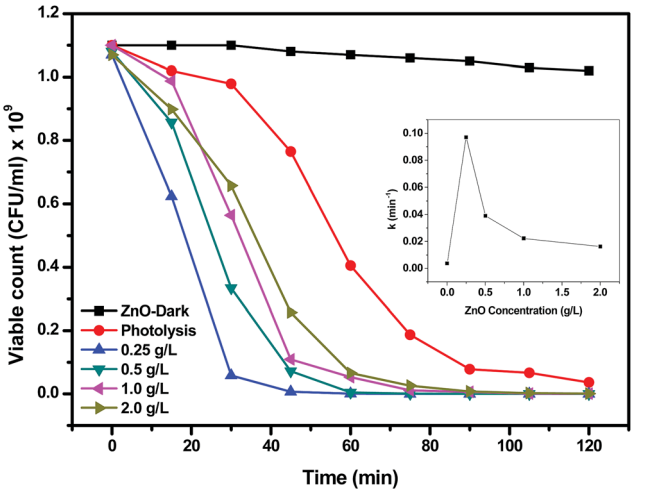

Fig. 7 Effect of ZnO concentration on the inactivation of *E. coli* under solar light. The inset represents the variation of rate constant in the presence of different concentrations of ZnO. (*E. coli* concentration: ~1 × 10^9 CFU mL^{-1}).

The effect of catalyst loading in the present study was investigated by incubating *E. coli* (at an initial cell number of approximately ~10^9 CFU mL^{-1}) in the presence of various concentrations of ZnO (varying form 0.25 mg mL^{-1} to 2.0 mg mL^{-1}) under sunlight and the results are shown in Fig. 7. The inset in the figure shows the rate constants under different catalyst loading. It may be mentioned here that appropriate control experiments in the presence of only sunlight without catalyst (photolysis control) and catalyst alone without sunlight (dark control) were also carried out. It can be observed from the figure that the bacterial count remained almost unchanged in the dark experiment indicating no inactivation of bacteria in absence of sunlight. On the other hand, after 120 min of irradiation under sunlight, photolysis alone resulted in a 1.3 log reduction in the viable bacterial count. However, significant increase in bacterial inactivation was observed in the presence of 0.25 mg mL^{-1} ZnO catalyst which demonstrated 5.5-fold higher inactivation as compared to photolysis. However, increasing catalyst loading to 0.5 mg mL^{-1} resulted in slight decrease in bacterial inactivation with 0.2 log reduction in viable count than 0.25 mg mL^{-1} ZnO catalyst. At still higher catalyst loading of 1 mg mL^{-1} and 2 mg mL^{-1}, photocatalytic inactivation of bacteria further decreased and a 3 log reduction in bacterial count was noted for both the catalyst loading indicating the saturation of bacterial inactivation by the ZnO photocatalyst in the present study.

The reaction rate constant k in min^{-1} has been calculated following the kinetic equation: $-\ln(C/C_o) = kt$ where, C_o is the initial concentration, C is the concentration for given time interval, k is the reaction rate constant and t is the time for reaction. The t value has been considered 30 min for calculation of k as the photocatalytic reaction becomes almost stable after 30 min duration. The highest rate constant of 0.097 min^{-1} was achieved for 0.25 mg mL^{-1} ZnO loading supporting the inactivation profile with subsequent decrease in rate constant upon increasing the concentration of catalyst. The rate constant obtained with 0.25 mg mL^{-1} ZnO loading is nearly four times that obtained with 2 g L^{-1} loading of ZnO, as shown in the inset of the figure.

As mentioned in the previous reports, the photocatalytic inactivation of microorganisms depends on various parameters such as generation of reactive oxygen species (ROS), absorption of the irradiated light and influence of these on total biomass.[36] The maximum inactivation of *E. coli* observed at a catalyst loading of 0.25 mg mL^{-1} in the present study could be due to the high absorption of sunlight that leads to the generation of high amount of ROS that maximally interacted with the bacterial mass. On the other hand, the decrease in bacterial inactivation at higher catalyst loading could be attributed to the shadowing or screening effect causing attenuation of sunlight reaching to the bacterial cells as a result of high amount of catalyst present in the medium. This shadowing/screening effect has been reported by others in previous studies on the photocatalytic inactivation of a microorganism as well as degradation of chemical contaminants.[37,38] The results

presented in Fig. 7 demonstrated that a catalyst loading of 0.25 mg mL^{-1} was the most efficient in terms of photocatalytic inactivation of *E. coli* in the present system. Similar observations were found by Zhang *et al.* where 0.3 mg mL^{-1} of ZnO nanoparticles showed highest inactivation against *E. coli* and *S. aureus*[38] and 0.25 mg mL^{-1} of TiO_2 showed the highest inactivation.[35]

3.2.2. Effect of initial bacterial concentration. The study on the influence of initial cell concentration on the photocatalytic killing of *E. coli*, inactivation of bacteria by ZnO nanopowders under sunlight was conducted with a catalyst loading of 0.25 mg mL^{-1} varying initial cell number from 10^5 to 10^9 CFU mL^{-1}. Fig. 8 shows that, when the initial cell concentration was 10^9 CFU mL^{-1}, a 2 log reduction in the viable count of bacteria was observed within 30 min. On the other hand, a 2.5 log reduction was noted within this duration when the initial cell number ranged 10^7 to 10^8 CFU mL^{-1}. However, the bacteria got killed within 60–80 min for these concentrations. At lower concentration of 10^5–10^6 CFU mL^{-1}, the inactivation process was observed fast and 10–15 min was enough to kill the total amount of bacteria. Complete inactivation of *E. coli* was observed for initial cell number 10^5 CFU mL^{-1} within 30 min period. The decrease in bacterial inactivation with increased concentration can be attributed to the exhaustion of surface active sites due to opacity in solution that are responsible for catalytic inactivation.[39] The plot of reaction rate constant (k) *versus* initial bacterial concentration (CFU mL^{-1}) has been represented as inset in the figure. The results support that the reaction rate constant is nearly independent of the initial concentration.

3.2.3. Effect of H_2O_2 addition. A reaction *via* photocatalysis involves highly active $^{\bullet}OH$ radicals that are considered to oxidize various chemicals and microorganisms. Generation of hydroxyl radicals takes place through hydrogen peroxide as an intermediate. H_2O_2 is a well-known disinfectant and therefore, plays major role during the photochemical reactions leading to high rates of reaction in its presence. In the present system, suspension of catalyst-*E. coli* with H_2O_2 addition, high rates of bacterial inactivation is expected due to more radical formation.[40] An optimum ZnO catalyst concentration of 0.25 mg mL^{-1} was loaded to the bacterial solution having concentration 1×10^9 CFU mL^{-1}. The results of H_2O_2 addition have been represented in Fig. 9 and the inset presents the plot of reaction rate constant *versus* concentration of H_2O_2. A control experiment has been performed with 10 mM of H_2O_2 under sunlight without catalyst. It showed 2.5-log reduction in the viable count. A slight increase in bacterial inactivation was observed as the H_2O_2 concentration varied from 1 mM to 5 mM. With an increase in the H_2O_2 concentration to 20 mM, the bacterial killing ability of ZnO also increased within time period of 60 min with viable count to 5.7 log reduction. A further increase to 100 mM enhanced the inactivation to 6.2-log reduction in the viable count. Thus, the results suggest that improvement in bacterial inactivation is found with addition of H_2O_2 in comparison to inactivation without the presence of disinfectant.[41] The inset kinetic plot clearly depicts the increase in rate constant with an increase in the molar concentration of H_2O_2. A nearly linear increase in the reaction rate with H_2O_2 concentration is observed initially. The reaction rate becomes constant after a concentration of 10 mM. This suggests that production of hydroxyl radicals at 10 mM is sufficient for the effective inactivation of bacteria.

3.2.4. Photocatalytic efficacy of different catalysts. In order to compare the photocatalytic efficacies of different catalysts, photocatalytic inactivation of *E. coli* was examined in presence of 0.25 mg mL^{-1} of various catalysts namely ZnO, ZnO–Ag (sub) and ZnO–Ag (imp) under sunlight or dark condition for 2 h as shown in Fig. 10. The inset bar graph in the figure shows the reaction rate constant for different catalysts under dark and visible sunlight. In absence of sunlight (dark), ZnO did not show any significant photocatalytic inactivation while ZnO–Ag (sub)

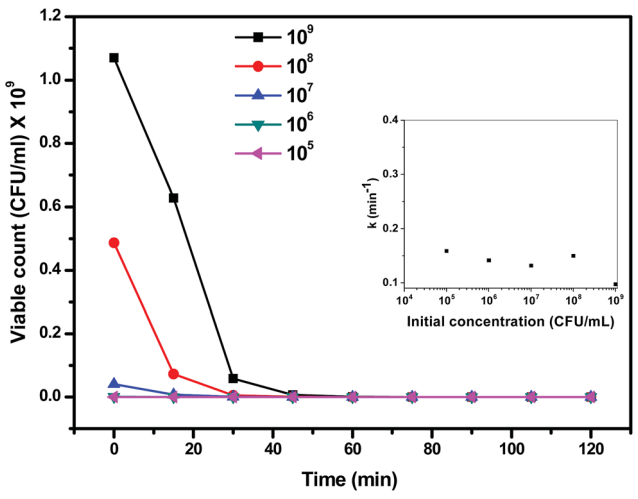

Fig. 8 Effect on inactivation with different initial *E. coli* concentrations. The inset represents the plot of rate constant at various *E. coli* initial concentrations. (Catalyst concentration: 0.25 g L^{-1}).

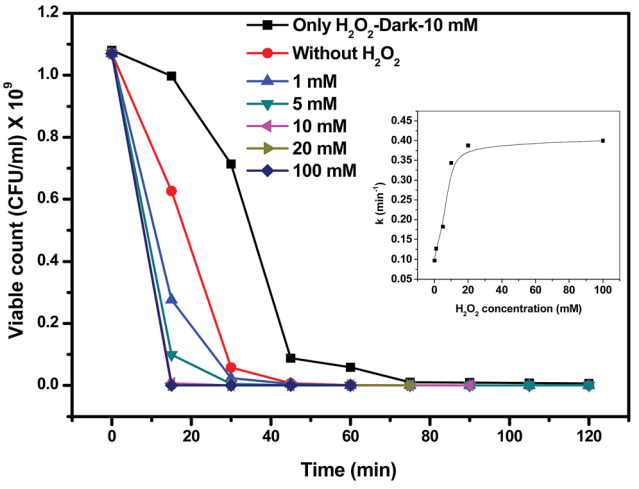

Fig. 9 Effect of H_2O_2 addition on the photocatalytic inactivation of *E. coli* by ZnO. The inset shows the plot of rate constant with H_2O_2 concentration. (Catalyst concentration: 0.25 g L^{-1}, *E. coli* concentration: ~1×10^9 CFU mL^{-1}).

and ZnO–Ag (imp) demonstrated 1 and 2 log reduction, respectively, in bacterial count. Under the sunlight, all the three synthesized catalysts exhibited significant photocatalytic inactivation with the maximum inactivation potential shown by ZnO–Ag (imp) with 6.7 log reduction followed by ZnO–Ag (sub) showing 5.9 log reduction and ZnO showing only 5.1 log reduction. ZnO–Ag (imp) was found to be the best among the synthesized catalyst and was actually as potential as commercial catalyst in terms of photocatalytic killing of bacteria. The above results are justified by the reaction rate constants as shown in the inset of the Fig. 10. Addition of silver also affects in the dark for bacterial killing with lower rate constants. There is a gradual increase in the rate of reaction with addition of Ag. Similar trend is followed in both dark and sunlight. The reaction rate constants for ZnO, ZnO–Ag (sub) and ZnO–Ag (imp) catalysts are found to be 0.097 min^{-1}, 0.16 min^{-1} and 0.26 min^{-1} under sunlight, respectively. However, Ag impregnated ZnO shows highest rate constant attributing to effective charge separation *via* impregnation of silver. The mechanism has been explored in the later section. The enhancement of photoactivity can be attributed to the superior physical and chemical properties due to the synthesis process. The combustion synthesized ZnO catalyst has high porous structure leading to higher surface area of 16.8 m^2 g^{-1} and also holds high moisture content. The substitution of silver decreases the surface to 14.2 m^2 g^{-1} and impregnated silver further reduces to 12.4 m^2 g^{-1}. Reduced surface area do not have significant effect. However, both silver substituted and impregnated shows synergistic effect due to reaction of reactive oxidative species and bacterium contact with silver is equally important. Silver is known to cause disruption of cell wall and its membrane. However, the photoactivity of silver substitution was observed lower due to radiation free recombination of charge carriers.[42] On the other hand, impregnation of the metallic Ag in ZnO generates oxide ion vacancies that act like electron-trapping sites that are the prime reason for higher inactivation of bacteria *via* ZnO–Ag (imp). Very recently, Ag@ZnO nanostructures were mediated onto cotton fabrics for visible light driven activities and also antimicrobial activities by Manna *et al.* A variation in silver nitrate concentration in ZnO matrix showed difference in microbial killing. However, Ag@ZnO particles having the silver precursor concentration of 2.5×10^{-5} M showed highest bacterial killing but higher concentration led to decrease in antimicrobial functionality.[43]

As explained in Section 2.7, deactivation studies were conducted with ZnO–Ag (imp) for seven cycles. It is clearly observed from Fig. 10 that no significant deactivation was observed and the bacterial inactivation remained almost similar to the first cycle.

As discussed in Section 2.2, bacterial inactivation was also examined for Ag impregnated ZnO wherein ZnO was obtained commercially. Fig. 10 shows this catalyst, ZnO–Ag imp (comm), shows activity for bacterial inactivation that is higher than that of ZnO but is lower than that of ZnO–Ag imp prepared in this study. This clearly shows the superior activity of Ag impregnated ZnO prepared by solution combustion compared to the Ag impregnated commercial ZnO.

3.2.5. Photocatalytic mechanism. The above results showed that ZnO–Ag (imp) had significantly increased the photocatalytic activity. This enhanced activity could be attributed to structural and physical features such as high porous and open nanostructured surface layer and also the presence of silver. There is an increase in the catalytically active sites and oxygen defects that reduces the charge recombination. These special features facilitate the easy photochemical reaction due to high mobility of oxidative species. Fig. 11(a) illustrates the proposed band structure and charge transfer mechanism in ZnO–Ag structure along with process of bacteria killing. The accepted photochemical theory predicts that, an electron excitation takes place from VB to CB leaving behind a hole, when a photon having energy of $h\nu$ equals or exceeds the energy band gap of the semiconductor. However, these photogenerated electron and hole pairs can recombine and dissipate the input energy as heat. This recombination is prevented by suitable surface defect states or scavengers *via* trapping of electron or hole. The hydroxyls groups on the surface also play an important role in trapping of photogenerated electron or hole and actively participate in the reaction. Formation of superoxide anion experiences acid–base equilibrium to contend with the adsorbed water molecules for photogenerated holes and becomes precursor for hydroxyl radicals.[44] These reactive oxidative species such as peroxide and hydroxyl radicals inhibit the lag phase of bacterial growth *via* disruption of cell membrane. They invade DNA structure to stop the functioning of minerals, proteins and genetic materials that are leaked due to cell wall disruption causing ultimate cell death as shown in Fig. 11(b).

A better outlook to the functioning of photocatalysts can be given by PL analyses. Photoluminescence spectroscopy is one of the powerful tools in characterization of the optical properties of semiconductor materials. Fig. 12 shows the photoluminescence spectra of ZnO, Ag substituted ZnO and Ag

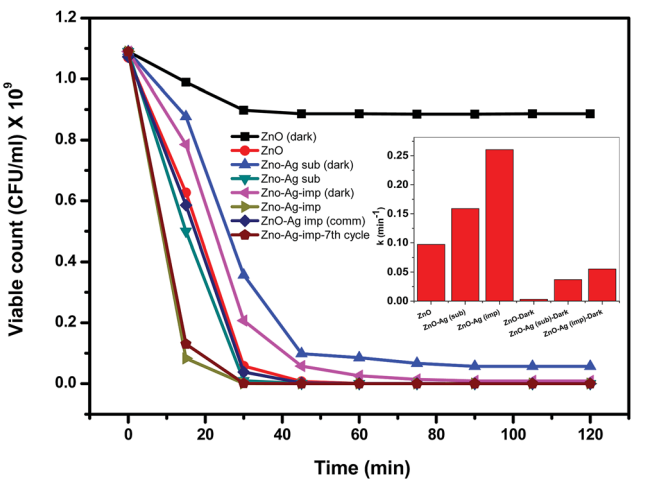

Fig. 10 Effect of different catalyst on the inactivation of *E. coli*. The inset represents the plot of rate constant with different catalysts under dark and on exposure to solar radiation. (Catalyst concentration: 0.25 mg mL^{-1}, *E. coli* concentration: ~1×10^9 CFU mL^{-1}).

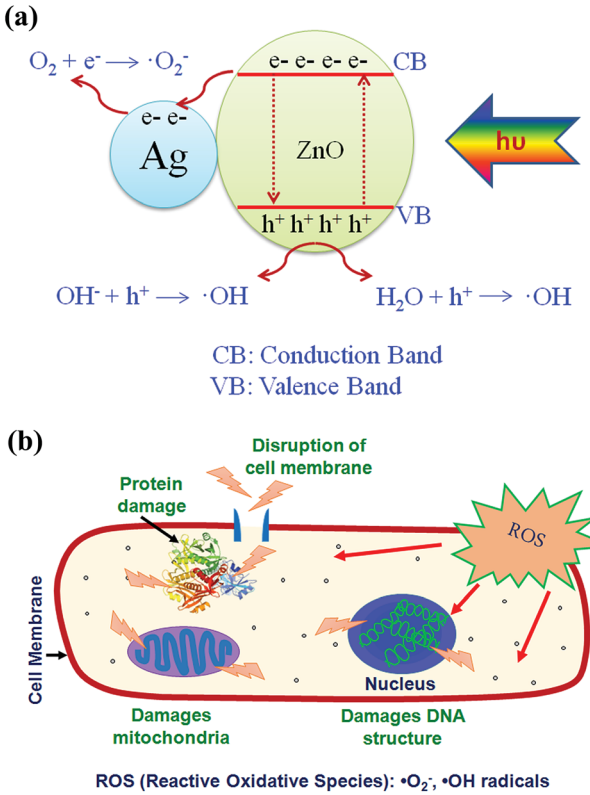

Fig. 11 Proposed schematic of (a) photocatalytic mechanism for Ag impregnated ZnO and (b) process of *E. coli* disruption.

impregnated ZnO. Room temperature excitation of zinc oxide nanoparticles at 325 nm shows photoluminescence at both UV and visible regions. However, UV emission corresponds to band gap of the zinc oxide nanoparticles, visible region emission should be noted with regard to Ag substitution and impregnation. The visible range emission is owed to the presence of oxygen defects and incorporation of silver into zinc oxide. The increase in emission of Ag substituted zinc oxide at visible region is due to that Ag^+ ions has got substituted into Zn^{2+} lattice creating ionized oxygen vacancies. The Ag impregnated zinc oxide sample showed less photoluminescence intensity compared to substituted and pristine zinc oxide samples. This is because the impregnated Ag exists as such in metallic state associated with zinc oxide nanoparticles. Therefore, whenever zinc oxide gets excited, the charge carriers get separated by the metallic Ag which acts as electron sink and decrease the recombination.[45] Hence, silver impregnated zinc oxide shows better photoactivity compared to pristine and Ag substituted zinc oxide catalysts.

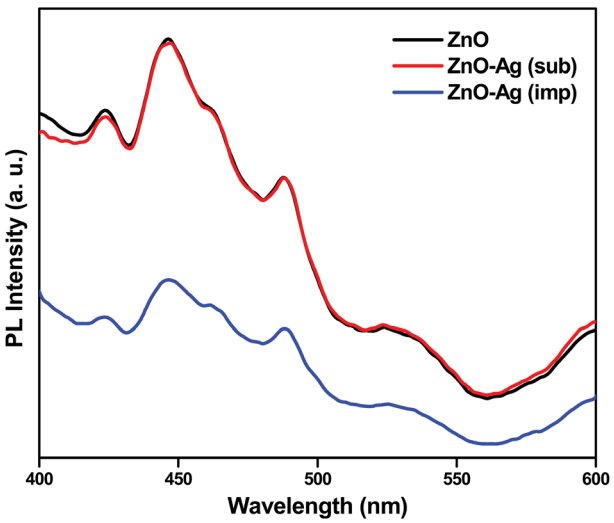

Fig. 12 PL spectra of pristine ZnO, ZnO–Ag (sub) and ZnO–Ag (imp) nanopowders.

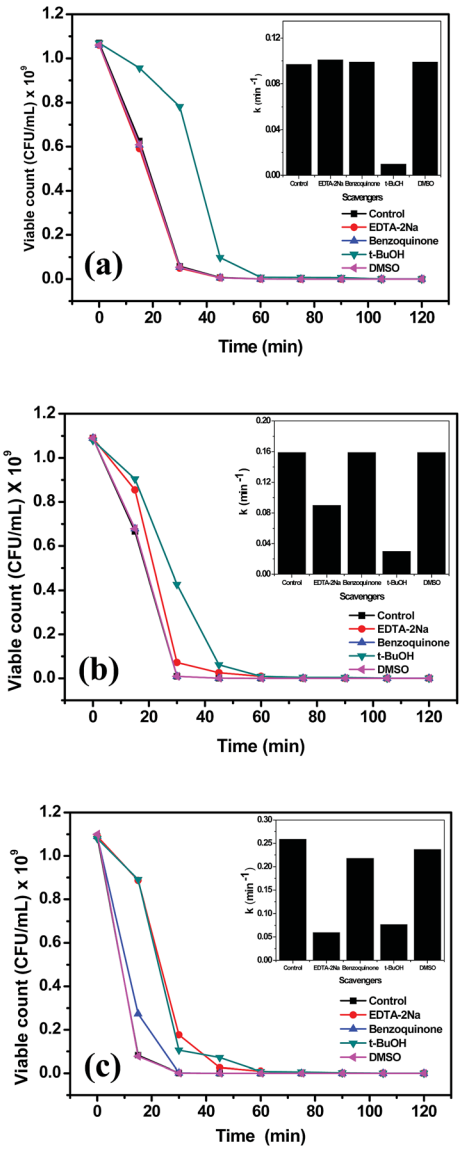

Fig. 13 Photogenerated carrier trapping in the systems of *E. coli* inactivation over (a) ZnO, (b) ZnO–Ag (sub) and (c) ZnO–Ag (imp), respectively, with different scavengers such as EDTA–2Na, benzoquinone, *t*-BuOH and DMSO. The inset shows the variation of rate constant in the presence of different scavengers.

The proposed mechanism can be supported by the photochemical experiments by means of trapping agents for radicals and holes. Scavengers used were EDTA–2Na (hole scavenger), benzoquinone ($^{\bullet}O_2^-$ radical scavenger), *t*-BuOH ($^{\bullet}$OH radical scavenger) and DMSO (electron scavenger). Control experiments were carried out only with the designated catalyst for bacterial inactivation. Fig. 13(a) shows the plot of viable bacterial count with time variation of the different reaction systems containing scavengers with pristine zinc oxide catalyst. The inset in the figure shows the rate constants in the presence of different scavengers. The reduced rate constant confirms the trapping of hydroxyl radicals by *t*-BuOH produced during the reaction. It suggests that the main oxidative species are $^{\bullet}$OH radicals. Hydroxyl radical scavengers greatly influence the bacterial killing. Fig. 13(b) and (c) show the viable count plot of Ag substituted and impregnated zinc oxide in the presence of different scavengers, respectively. Both EDTA–2Na and *t*-BuOH shows effective trapping of hole and $^{\bullet}$OH radical. This can be predicted that silver acts as sink for the electrons whereas hole reduces the hydroxyl ion on the surface to produce hydroxyl radical that further promotes the photochemical reaction for bacterial killing.[27] The insets in Fig. 13(b) and (c) support the hole and radical trapping with lowest rate constants observed for EDTA–2Na and *t*-BuOH scavengers. However, rate constant for impregnated silver (0.06 min^{-1}) is less than substituted silver (0.09 min^{-1}) supporting the better activity of Ag impregnated ZnO in the presence of scavenger. It is observed that both hole and hydroxyl radical scavenger have nearly equal constants supporting the above result. This suggests that the hole and surface hydroxyls play very crucial role in the photocatalytic killing of bacteria.

4. Conclusions

Successful synthesis of hexagonal wurtzite ZnO was carried having BET surface area of 16.8 $m^2\ g^{-1}$. A modification to ZnO was performed by Ag substitution and impregnation bearing surface area of 14.2 $m^2\ g^{-1}$ and 12.4 $m^2\ g^{-1}$, respectively. Substitution and impregnation of silver as Ag^+ ion and metallic Ag was confirmed from XPS. The photocatalytic tests showed that Ag impregnated ZnO exhibits excellent bacterial inactivation. The porous and open structure of ZnO favored the effective inactivation by increasing the number of active sites and effective charge separation observed in presence of Ag. Ag acts as an electron sink and hole as hydroxyl radical former for the photochemical killing of bacteria. The experiments for different radical and electron–hole trapping showed that the photogenerated holes and $^{\bullet}$OH radicals are the main oxidative species for *E. coli* inactivation.

Acknowledgements

This research work was financially supported by NRCM, IISc. Bangalore. The authors would like to acknowledge Ms. Shreya Shetty for conducting preliminary experiments, Mr. Satyapaul Singh for helpful discussion on XRD and Ms. Leelavathi Annamalai for discussion on TEM. The authors gratefully acknowledge the Centre of Nanoscience and Engineering for characterization facilities.

References

1 C. Wang, Y. Ao, P. Wang, J. Hou and J. Qian, *Colloids Surf., A*, 2014, **360**, 184–189.
2 Y. R. Smith, A. Raj, K. Joseph, V. Ravi Subramanian and B. Viswanathan, *Colloids Surf., A*, 2010, **367**, 140–147.
3 A. Fujishima, T. N. Rao and D. A. Tryk, *J. Photochem. Photobiol., C*, 2000, **1**, 1–21.
4 O. Yamamoto, *Int. J. Inorg. Mater.*, 2001, **3**, 643–646.
5 L. Fiksdal, I. Tryland and H. Nelis, *Water Sci. Technol.*, 1997, **35**, 415–418.
6 R. Brayner, R. Ferrari-Iliou, N. Brivois, S. Djediat, M. F. Benedetti and F. Fiévet, *Nano Lett.*, 2006, **6**, 866–870.
7 R. Asahi, T. Morikawa, T. Ohwaki, K. Aoki and Y. Taga, *Science*, 2001, **293**, 269–271.
8 S. Krishnan, T. Chinnasamy, S. Veerappan, K. Senthilkumar and D. Kannaiyan, *Mater. Sci. Eng., C*, 2014, **45**, 337–342.
9 K. H. Tam, A. B. Djurisic, C. M. N. Chan, Y. Y. Xi, C. W. Tse, Y. H. Leung, W. K. Chan, F. C. C. Leung and D. W. T. Au, *Thin Solid Films*, 2008, **516**, 6167–6174.
10 H. Shi, G. Li, H. Sun, T. An, H. Zhao and P. K. Wong, *Appl. Catal., B*, 2014, **158**, 301–307.
11 Z. Wang, *J. Phys.: Condens. Matter*, 2004, **16**, 829–858.
12 H. Song, H. Yang and X. Ma, *J. Alloys Compd.*, 2013, **578**, 272–278.
13 S. Sharma, R. Vyas, N. Sharma, V. Singh, A. Singh, V. Kataria, B. Kumar Gupta and Y. K. Vijay, *J. Alloys Compd.*, 2013, **552**, 208–213.
14 H. Li, Z. Zhang, J. Huang, R. Liu and Q. Wang, *J. Alloys Compd.*, 2013, **550**, 526–530.
15 M. Zhang, F. Jin, M. Zheng and J. Liu, *RSC Adv.*, 2014, **4**, 10462–10466.
16 L. Zhang, Y. Ding, M. Povey and D. York, *Prog. Nat. Sci.*, 2008, **18**, 939–944.
17 J. Das and D. Khushalani, *J. Phys. Chem. C*, 2010, **114**, 2544–2550.
18 A. Hagfeldt and M. Gratzel, *Chem. Rev.*, 1995, **95**, 49–68.
19 Y. Liu, J. Yang, Q. Guan, L. Yang, H. Liu, Y. Zhang, Y. Wang, D. Wang, J. Lang, Y. Yang, L. Fei and M. Wei, *Appl. Surf. Sci.*, 2010, **256**, 3559–3562.
20 L. Zhang, Y. Jiang, Y. Ding, N. Daskalakis, L. Jeuken, P. Malcolm, A. J. O'Niell and D. W. York, *J. Nanopart. Res.*, 2010, **12**, 1625–1636.
21 Y. Zheng, C. Chen, Y. Zhan, X. Lin, Q. Zheng, K. Wei and J. Zhu, *J. Phys. Chem. C*, 2008, **112**, 10773–10777.
22 M. K. Lee, T. G. Kim, W. Kim and Y. M. Sung, *J. Phys. Chem. C*, 2008, **112**, 10079–10082.
23 K. Nagaveni, G. Sivalingam, M. S. Hegde and G. Madras, *Environ. Sci. Technol.*, 2004, **38**, 1600–1604.
24 K. C. Patil, M. S. Hegde, T. Rattan and S. T. Aruna, *Chemistry of nanocrystalline oxide materials-combustion synthesis, properties and applications*, World Scientific, New Jersey, 2008, pp. 1–20.

25 T. Sun, J. Qiu and C. Liang, *J. Phys. Chem. C*, 2008, **112**, 715–721.
26 Z. Li, F. Zhang, A. Meng, C. Xie and J. Xing, *RSC Adv.*, 2015, **5**, 612–620.
27 Y. Cai, H. Fan, M. Xu and Q. Li, *Colloids Surf., A*, 2013, **436**, 787–795.
28 S. Sontakke, J. Modak and G. Madras, *Appl. Catal., B*, 2011, **106**, 453–459.
29 K. Nagaveni, G. Sivalingam, M. S. Hegde and G. Madras, *Appl. Catal., B*, 2004, **48**(2), 83–93.
30 R. S. Zeferino, M. B. Flores and U. Pal, *J. Appl. Phys.*, 2011, **109**, 14308.
31 J. M. Liu, C. K. Ong and L. C. Lim, *Ferroelectrics*, 1999, **231**, 223–229.
32 C. Gu, C. Cheng, H. Huang, T. Wong, N. Wang and T. Zhang, *Cryst. Growth Des.*, 2009, **9**, 3278–3285.
33 D. Lin, H. Wu, R. Zhang and W. Pan, *Chem. Mater.*, 2009, **21**, 3479–3484.
34 N. Serpone, D. Lawless and R. Khairutdinov, *J. Phys. Chem.*, 1995, **99**, 16646–16654.
35 S. Sontakke, C. Mohan, J. Modak and G. Madras, *Chem. Eng. J.*, 2012, **189**, 101–107.
36 D. S. Bhatkhande, V. G. Pangarkar and A. A. Beenackers, *J. Chem. Technol. Biotechnol.*, 2002, **77**, 102–116.
37 A. K. Benabbou, Z. Derriche, C. Felix, P. Lejeune and C. Guillard, *Appl. Catal., B*, 2007, **76**, 257–263.
38 Y. Zhang, X. Gao, L. Zhi, X. Liu, W. Jiang, Y. Sun and J. Yang, *J. Inorg. Biochem.*, 2014, **130**, 74–83.
39 S. K. Mohanty and A. B. Boehm, *Environ. Sci. Technol.*, 2014, **48**, 11535–11542.
40 N. R. Asad, L. M. B. O. Asad, A. B. Silva, I. Felzenszwalb and A. C. Leitão, *Acta Biochim. Pol.*, 1998, **45**, 677–690.
41 O. Legrini, E. Oliveros and A. M. Braun, *Chem. Rev.*, 2002, **93**, 671–698.
42 R. van Grieken, J. Marugán, C. Sordo, P. Martínez and C. Pablos, *Appl. Catal., B*, 2009, **93**, 112–118.
43 J. Manna, S. Goswami, N. Shilpa, N. Sahu and R. K. Rana, *ACS Appl. Mater. Interfaces*, 2015, **7**, 8076–8082.
44 Y. Liu and H. Kim, *Carbohydr. Polym.*, 2012, **89**, 111–116.
45 C. Karunakaran, V. Rajeshwari and P. Gomathisankar, *J. Alloys Compd.*, 2010, **508**, 587–591.